Article

Emergent hydrodynamics in a strongly interacting dipolar spin ensemble

https://doi.org/10.1038/s41586-021-03763-1

Received: 22 September 2020

Accepted: 23 June 2021

Published online: 1 September 2021

Check for updates

C. Zu[1,2,7], F. Machado[1,2,7], B. Ye[1,7], S. Choi[1], B. Kobrin[1,2], T. Mittiga[1,2], S. Hsieh[1,2], P. Bhattacharyya[1,2], M. Markham[3], D. Twitchen[3], A. Jarmola[1,4], D. Budker[1,5], C. R. Laumann[6], J. E. Moore[1,2] & N. Y. Yao[1,2]✉

Conventional wisdom holds that macroscopic classical phenomena naturally emerge from microscopic quantum laws[1–7]. However, despite this mantra, building direct connections between these two descriptions has remained an enduring scientific challenge. In particular, it is difficult to quantitatively predict the emergent 'classical' properties of a system (for example, diffusivity, viscosity and compressibility) from a generic microscopic quantum Hamiltonian[7–14]. Here we introduce a hybrid solid-state spin platform, where the underlying disordered, dipolar quantum Hamiltonian gives rise to the emergence of unconventional spin diffusion at nanometre length scales. In particular, the combination of positional disorder and on-site random fields leads to diffusive dynamics that are Fickian yet non-Gaussian[15–20]. Finally, by tuning the underlying parameters within the spin Hamiltonian via a combination of static and driven fields, we demonstrate direct control over the emergent spin diffusion coefficient. Our work enables the investigation of hydrodynamics in many-body quantum spin systems.

Even in the absence of a precise microscopic description, classical hydrodynamics provides a powerful framework for characterizing the macroscopic behaviour of local, conserved quantities, such as energy. Understanding whether and how it emerges in the late-time dynamics of strongly interacting quantum systems remains an essential open question. For a quantum system coupled to an environment, it is unsurprising that the late-time behaviour becomes classical; indeed, dephasing from the bath destroys the intrinsic quantum coherences of the system. However, even for an isolated, many-particle quantum system, conventional wisdom holds that late-time dynamics usually exhibit an emergent classical description; understanding how to prove this fact and the required conditions has remained an enduringly hard question[7–13,21,22]. At the same time, it has also motivated seminal advances. On the theoretical front, precise analytic insights have been obtained in the context of integrable systems using generalized hydrodynamics and non-integrable systems using perturbative approaches[12,13,22–26]. On the experimental front, tremendous progress in time-resolved measurement techniques has enabled the direct observation of emergent classical diffusion in several classes of quantum system[2,3,27–31].

There are, however, a wide variety of classical dynamical 'universality classes' other than diffusion: aside from the simple case of free (ballistic) behaviour, two well known classes are Kardar–Parisi–Zhang dynamics and Sinai diffusion[32–35]. Here we report time-resolved experiments on a closed quantum system, which exhibits an unconventional approach to late-time diffusion characterized by a long-lived, non-Gaussian polarization profile.

Our experimental platform consists of two strongly interacting species of electronic spins in diamond: substitutional nitrogen defects (P1 centres) and nitrogen-vacancy (NV) colour centres[36,37]. By controlling the relative density of these two species, we demonstrate the ability to prepare inhomogeneous spatial profiles of a conserved spin density, as well as to locally probe the resulting nanoscale spin dynamics (Fig. 1). These dynamics can be tuned via three independent controls: (1) the initial spin polarization, (2) the average spacing between spins and (3) the magnitude of the on-site random fields.

Exploring this phase space leads us to an understanding of how the details of the microscopic spin Hamiltonian modify conventional diffusion. By tracking the local autocorrelation function of the spin polarization, $S_p(t)$, we observe the emergence of a long-time, diffusive power law, $S_p(t) \propto t^{-3/2}$, for over an order of magnitude in time t (Fig. 1b). However, the details of this autocorrelation function over a broad range of timescales indicate that, following local initialization, the spin polarization distribution remains non-Gaussian throughout the timescales accessible in the experiment; this originates from the presence of strong disorder in our system, which leads to a distribution of local diffusion coefficients and a Yukawa-like spin polarization profile (Fig. 1d).

Hybrid spin platform

We choose to work with samples containing a P1 density of about 100 ppm and an NV density of about 0.5 ppm, leading to a geometry where each spin-1 NV centre is surrounded by a strongly interacting ensemble of spin-1/2 P1 centres (Fig. 1a). In this geometry, the NV centre naturally plays the role of both a polarization source and a local probe for nearby P1 centres. These roles rely on two ingredients. First,

[1]Department of Physics, University of California, Berkeley, CA, USA. [2]Materials Science Division, Lawrence Berkeley National Laboratory, Berkeley, CA, USA. [3]Element Six, Harwell, UK. [4]US Army Research Laboratory, Adelphi, MD, USA. [5]Helmholtz Institut Mainz, Johannes Gutenberg Universitat Mainz, Mainz, Germany. [6]Department of Physics, Boston University, Boston, MA, USA. [7]These authors contributed equally: C. Zu, F. Machado, B. Ye. ✉e-mail: norman.yao@berkeley.edu

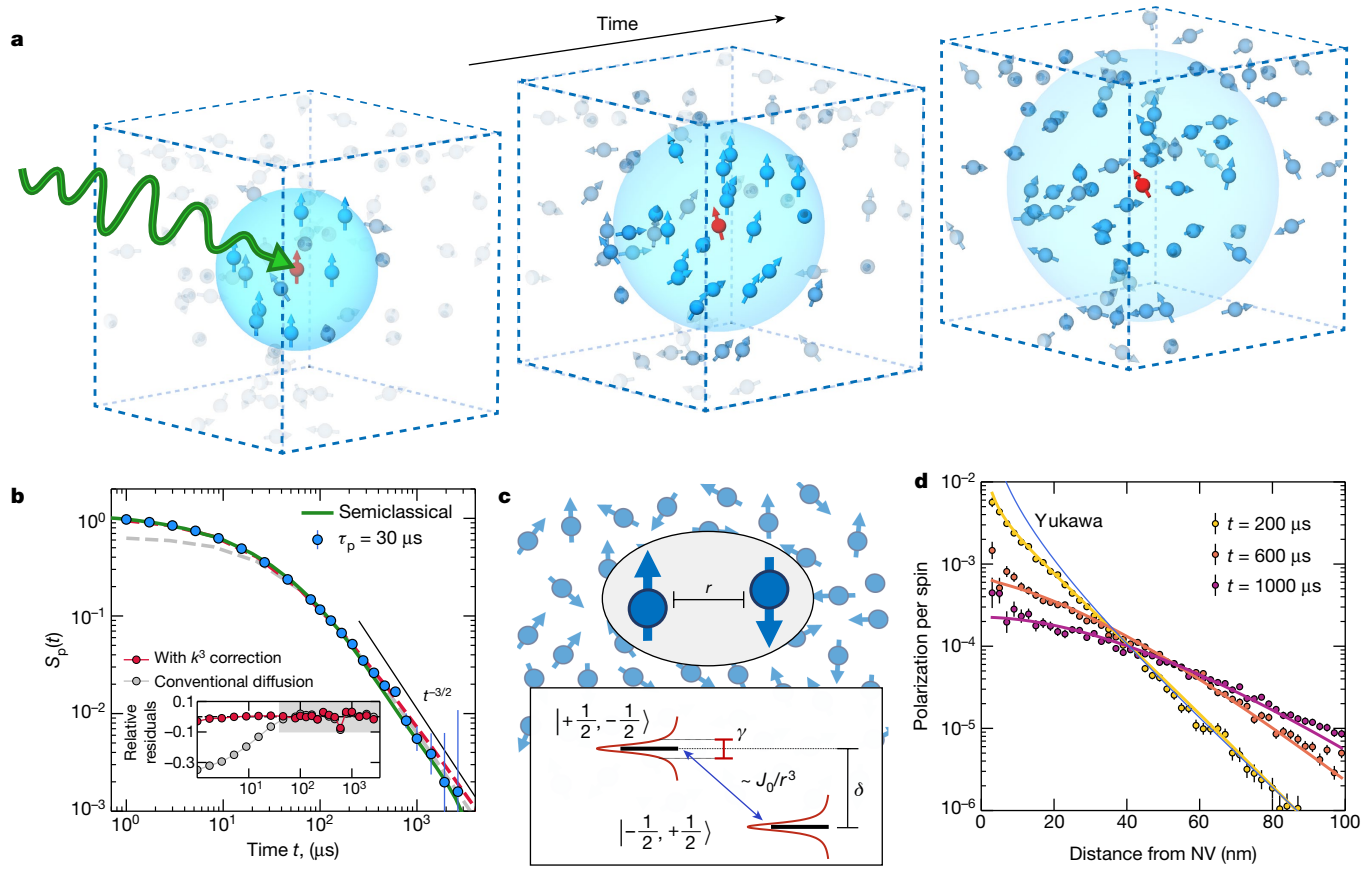

Fig. 1 | Nanoscale spin diffusion in a long-range interacting quantum system. **a**, Schematic depicting the emergence of hydrodynamics in a strongly interacting dipolar spin ensemble. Optical pumping (green arrow) of the NV centre (red) enables it to behave as a polarization source for nearby P1 centres (blue), resulting in the preparation of a local, inhomogenous spin-polarization profile. Dynamics then lead to the spreading of this profile as a function of time. **b**, Dynamics of the survival probability $S_p(t)$ of the $\nu = 1/3$ P1 subgroup in sample S2 at $T = 25$ K following a polarization period of $\tau_p = 30$ μs. After an initial transient, $S_p(t)$ approaches a robust power-law decay of $t^{-3/2}$, indicating diffusion. The late-time dynamics are accurately described by the diffusion equation (grey dashed line). The red dashed line corresponds to spin diffusion with an additional long-range correction $C_{lr}k^3$ (Methods, Extended Data Fig. 9). Inset: relative residuals for the two spin diffusion models. In the hydrodynamical regime (grey shaded region), both models capture the data. **c**, Illustration of our semiclassical description for the spin-polarization dynamics. Each pair of spins exchanges polarization via the dipolar interaction. The presence of other nearby P1 spins leads to an energy mismatch δ and a homogeneous broadening γ; these parameters are independently measured (Extended Data Fig. 4). **d**, Initializing with unit polarization, a robust non-Gaussian polarization profile emerges from the semiclassical model for all experimentally accessible timescales. The crossover from a Yukawa to a Gaussian polarization profile is accurately captured by including the disorder-induced dynamical modification, $C_{dyn}k^2\partial_t P_k$, in the diffusion equation, with $C_{dyn} = 204 \pm 45$ nm^3 (Methods, Extended Data Fig. 7). All errors represent 1 s.d. accounting statistical uncertainties.

the NV centre can be optically initialized (to $|m_s^{NV} = 0\rangle$, where m_s is the spin quantum number) and read out using green laser illumination, which does not affect the P1 centre. Second, the NV and P1 centres can coherently exchange spin polarization when brought into resonance via an external magnetic field (Fig. 2a)[37]; this polarization exchange is driven by the $\Delta m_s = \pm 2$ components of the magnetic dipole–dipole interaction:

$$H_{NV-P1} = -\sum_i \frac{J_0}{r_{NV,i}^3}(A_i[S^+P_i^+ + S^-P_i^-] + B_i S^z P_i^z), \quad (1)$$

where $J_0 = (2\pi) \times 52$ MHz nm^3 characterizes the strength of the dipolar interaction, $r_{NV,i}$ is the distance between the NV centre and the ith P1 centre, A_i and B_i capture the angular dependence of the dipolar interaction (Supplementary Information), and $S^{\pm}$ and $P^{\pm}$ are raising and lowering operators for the NV and P1, respectively. We note that H_{NV-P1} corresponds to the energy-conserving terms of the dipolar interaction, when restricting our attention to the NV spin subspace $\{|0\rangle, |-1\rangle\}$ (Fig. 2a).

In addition, the P1 centres also exhibit dipolar interactions among themselves driven by the $\Delta m_s = 0$ component:

$$H_{P1-P1} = -\sum_{i<j} \frac{J_0}{r_{i,j}^3}\left(\widetilde{A}_{i,j}\left[P_i^+P_j^- + P_i^-P_j^+\right] + \widetilde{B}_{i,j}P_i^zP_j^z\right) \quad (2)$$

where $\widetilde{A}_{i,j}$ and $\widetilde{B}_{i,j}$ are the analogous angular coefficients between the ith and jth P1s (Supplementary Information).

When the NV and P1 are off-resonant, we observe an NV depolarization timescale, $T_{depol} = 2.3 \pm 0.1$ ms, consistent with room-temperature, spin-phonon relaxation (Fig. 2b)[36]. By applying a magnetic field, $B = 511$ G, along the NV axis, the NV's $|0\rangle \leftrightarrow |-1\rangle$ transition becomes resonant with the P1's $|-\frac{1}{2}\rangle \leftrightarrow |+\frac{1}{2}\rangle$ transition (Fig. 2a), and we find that T_{depol} decreases by over two orders of magnitude to 8.9 ± 0.6 μs (Fig. 2b)[37]. We emphasize that the reduced T_{depol} should not be thought of as extrinsic decoherence, but rather as a consequence of coherent NV–P1 interactions (Fig. 2e).

Local spin polarization

By continuously repolarizing the NV centre via green laser excitation, one can use H_{NV-P1} to transfer spin polarization to nearby P1 centres;

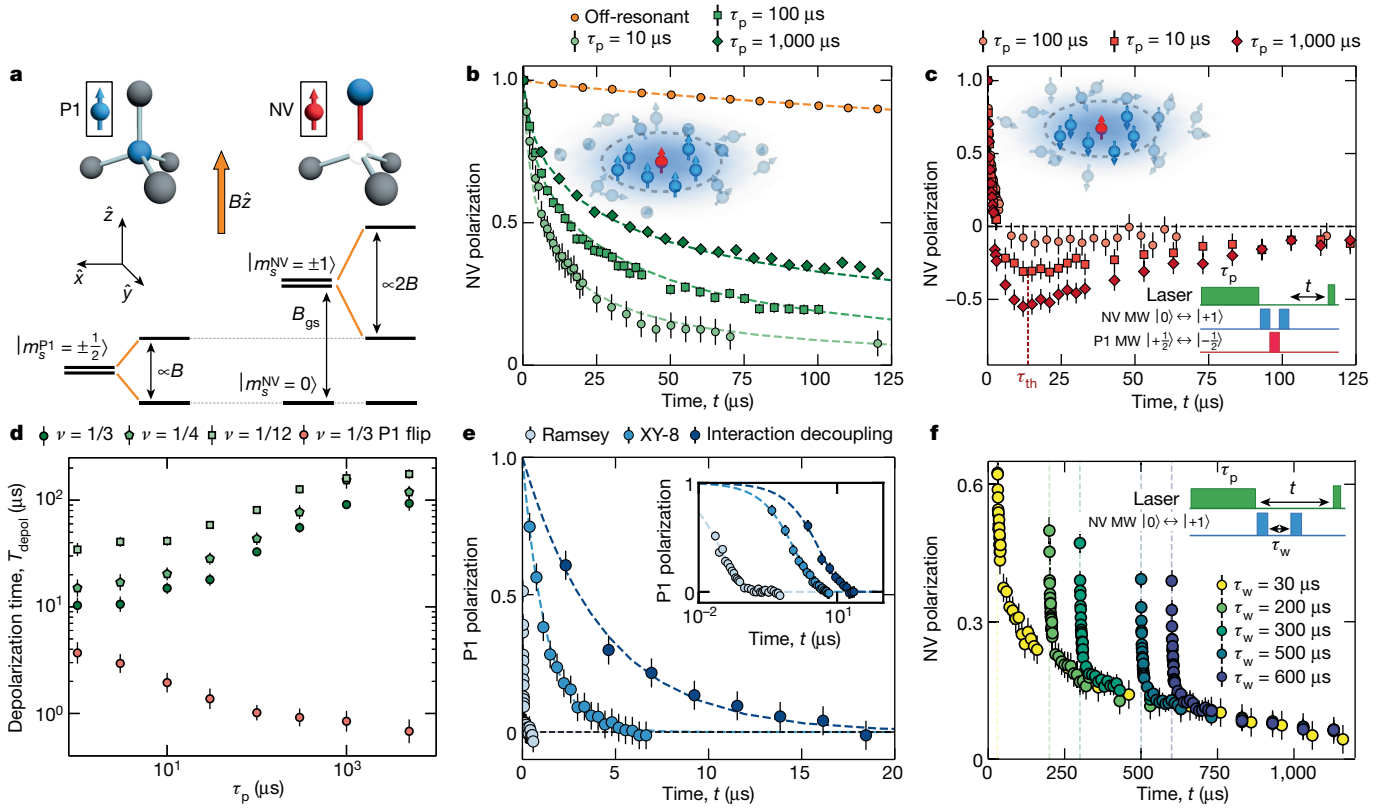

Fig. 2 | Probing local spin-polarization dynamics using the NV centre. **a**, In the absence of a magnetic field, the P1's spin-1/2 sublevels are degenerate, whereas the NV's spin-1 sublevels exhibit a zero field splitting, $D_{gs} = (2\pi) \times 2.87$ GHz. By applying an external magnetic field, the P1 and NV centre can be brought into resonance. **b**, When the NV and P1 are off-resonant (orange), $B = 360$ G, the NV exhibits a stretched exponential decay of about $e^{-(t/T_1^{NV})^{0.8}}$ (dashed line) with $T_1^{NV} = 2.3 \pm 0.1$ ms, consistent with spin–phonon relaxation. When the NV is resonant with the $\nu = 1/3$ subgroup of P1s (green), $B = 511$ G, depolarization occurs much more rapidly and is strongly dependent upon the polarization time τ_p; a longer τ_p leads to a larger local polarization of P1 centres (inset) and a correspondingly longer NV relaxation time. The dashed green lines correspond to the NV dynamics as captured by our semiclassical model (Methods). **c**, NV depolarization dynamics with an anti-polarized $\nu = 1/3$ P1 ensemble (top inset). Depolarization occurs in two distinct steps: an initial decay, $t \lesssim \tau_{th} \approx 12$ μs, corresponding to local equilibration with the P1 ensemble, followed by late-time diffusion. Bottom inset: the pulse sequence describes the preparation of the anti-polarized P1 ensemble via the application of laser light (green) and microwave pulses (MW, blue and red). **d**, Depolarization time, T_{depol} (extracted as the 1/e decay time of the initial polarization), as a function of τ_p for different effective P1 densities ν. The anti-polarized case for $\nu = 1/3$ is denoted as P1 flip (**c** above). As τ_p approaches P1's $T_1 \approx 1$ ms, T_{depol} saturates. **e**, P1 spin coherence time, T_2, for different dynamical decoupling sequences, Ramsey (0.032 ± 0.005 μs), XY-8 (1.27 ± 0.02 μs)] and an interaction decoupling sequence (4.4 ± 0.1 μs using DROID; Extended Data Fig. 1); coherence times are extracted from single exponential fits (dashed blue lines). Inset: data plotted in semi-log. **f**, Depolarization dynamics for $\tau_p = 1{,}000$ μs with variable NV-shelving time, τ_w (inset). The τ_w-independent collapse of the late-time data confirms the NV's role as a local probe of the P1's polarization dynamics. All data are taken using sample S1 at room temperature $T \approx 300$ K. Errors represent 1 s.d. accounting statistical uncertainties.

this polarization is further spread-out among the P1s by H_{P1-P1}. The duration of the laser excitation, τ_p, then controls the amplitude, shape and width of the local spin polarization. A longer τ_p leads to a larger local P1 polarization, which acts as a 'frozen core' around the NV centre (Fig. 2b, inset), suppressing dipolar spin exchange from H_{NV-P1}[38]. This suppression suggests that T_{depol}, measured after P1 polarization, should be substantially enhanced. This is indeed borne out by the data. As shown in Fig. 2b, d, T_{depol} is extended by an order of magnitude as a function of increasing τ_p. The increase saturates as τ_p approaches the spin–phonon relaxation time and the polarization process reaches a steady state (Fig. 2d)[39].

Probing nanoscale spin dynamics

To study the long-time dynamics associated with the dipolar-induced spreading of our initial polarization profiles, it is essential to distinguish between early-time local equilibration and late-time emergent dynamics. To this end, we introduce an experimental technique that allows us to explicitly observe local thermalization. In particular, after polarizing for τ_p, we utilize a microwave π-pulse to shelve the NV population from $|0\rangle$ into the highly off-resonant $|+1\rangle$ state (Fig. 2c, bottom inset). Next, we perform a global microwave π-pulse on the $|-\frac{1}{2}\rangle \leftrightarrow |+\frac{1}{2}\rangle$ P1 transition, flipping the ensemble's spin polarization. Finally, we unshelve the NV population, effectively preparing an initial condition where the NV is antipolarized relative to the P1 ensemble (Fig. 2c, top inset).

The dynamics starting from this antipolarized configuration are markedly distinct. First, the NV polarization quickly changes sign and reaches a negative value, indicating local thermalization with the oppositely oriented P1 ensemble. Second, the larger the antipolarization (controlled by τ_p), the faster the NV initially decays (Fig. 2c, d). Crucially, this allows us to extract a characteristic timescale for local thermalization, $\tau_{th} \approx 12$ μs.

Returning to the polarized case, we can now leverage the shelving technique to experimentally isolate the emergent late-time dynamics. In particular, we polarize for time τ_p, shelve the NV and then wait for a variable time τ_w to allow the P1 polarization to spread. Upon unshelving the NV, we observe a two-step relaxation process, as depicted in Fig. 2f. After an initial step of rapid local equilibration, the late-time dynamics exhibit a τ_w-independent collapse. Crucially, this demonstrates that for $t > \tau_{th}$, the NV polarization functions as a local probe of the amplitude

Table 1 | Spin diffusion coefficients across all samples, temperatures, P1 densities and disorder strengths.

Effective density	$\nu = 1/3$		$\nu = 1/4$		$\nu = 1/12$
Sample	S1	S2	S1 Ω_{drive} = 0 MHz	S1 $\Omega_{drive} = (2\pi) \times 11.7$ MHz	S1
D (nm^2 μs^{-1})	0.28 ± 0.06	0.35 ± 0.05	0.25 ± 0.06	0.33 ± 0.09	0.11 ± 0.03
gD (nm^2 μs^{-1})	0.82 ± 0.17	1.03 ± 0.13	0.74 ± 0.18	0.95 ± 0.26	0.33 ± 0.08
$D_{\langle r^2\rangle}$(nm^2 μs^{-1})	0.98 ± 0.03	1.09 ± 0.02	0.66 ± 0.04	0.95 ± 0.02	0.21 ± 0.03

Accounting for the appropriate non-Gaussian geometric factor, $g = 2\pi^{1/3}$, yields agreement between the diffusion coefficient extracted from the survival probability and that extracted from the growth of $\langle r^2\rangle$ (computed via our semiclassical model). Samples S1 and S2 both contain a P1 density of 110 ppm, and their NV densities are 0.7 ppm and 0.3 ppm, respectively (Supplementary Information). Measurements on S1 are performed at room temperature and measurements on S2 are taken at $T = 25$ K. For sample S1, we also consider two additional tuning parameters: (1) different effective P1 densities, $\nu \in \{1/3, 1/4, 1/12\}$, tuned via the hyperfine structure (Fig. 3c), and (2) different disorder strengths, W, tuned via continuous microwave driving (Fig. 3d). The reported uncertainties include propagated uncertainties from other experimentally extracted parameters (for example, T_1 and ρ_{NV}). Despite overlapping error bars, a detailed analysis (Supplementary Information) confirms that the driven diffusion coefficient is statistically larger than the undriven case. Errors represent 1 s.d. accounting statistical uncertainties.

of the P1 polarization profile, $P(t, \mathbf{r})$, at position $\mathbf{r}$; alternatively, one can also think of the NV's polarization as an autocorrelation function that captures the survival probability of the P1's polarization dynamics[40].

Observation of emergent diffusion

At late times, the conservation of total polarization and the dynamical exponent $z = 2$ determine the characteristic behaviour of the survival probability in d dimensions, $S_p(t) \propto t^{-d/2}$; the simplest hydrodynamic model capturing this corresponds to Gaussian diffusion:

$$\partial_t P(t, \mathbf{r}) = D\nabla^2 P(t, \mathbf{r}) - \frac{P(t, \mathbf{r})}{T_1} + Q(t, \mathbf{r}), \tag{3}$$

where D is the diffusion coefficient. The latter two terms in equation (3) are motivated by our experiment: $Q(t, \mathbf{r})$ is a source term that characterizes the P1 polarization process and T_1 is an extrinsic relaxation time, after which the experimental signal becomes suppressed (Methods). To maximize the experimental window for observing emergent hydrodynamics, we work at low temperatures $T = 25$ K, where the NV's T_1^{NV} time extends by an order of magnitude, and the P1's T_1 time extends by a factor of three (Methods, Extended Data Fig. 3)[41]. The source $Q(t, \mathbf{r})$ contains contributions from each of the randomly distributed NVs, whose finite density produces an overall uniform background polarization that decays exponentially in time. Isolating the nanoscale polarization dynamics from this background (Methods), we observe a robust power-law decay of the survival probability, $S_p(t) \propto t^{-3/2}$, for over a decade in time, demonstrating the emergence of spin diffusion (Fig. 1b)[40]. Extracting the corresponding diffusion coefficient from $S_p(t) = P_{total}/(4\pi Dt)^{3/2}$ requires one additional piece of information, namely, the total amount of spin polarization, P_{total}, transferred to the P1 ensemble. Fortunately, this is naturally determined by combining the height of the measured polarization background with the density of NVs, which we independently calibrate using a spin-locking experiment (Supplementary Information). This enables us to experimentally extract the spin-diffusion coefficient: $D = 0.35 \pm 0.05$ nm^2 μs^{-1} (Table 1).

An unconventional approach to diffusion

Although the hydrodynamic model in equation (3) captures the correct dynamical exponent, it assumes that the dynamics follow Gaussian diffusion at all times. However, disorder induces important modifications to this picture and leads to a novel dynamical correction. In particular, around each P1 centre there is a distinct local environment, arising from both positional disorder and the presence of on-site random fields (generated by other paramagnetic spin defects; Supplementary Information). This leads to a spatially varying local diffusion coefficient. As an initial polarization profile spreads, its dynamics naturally average over an increasing number of local P1 environments. This generates a dynamical modification to the diffusion equation, whose leading contribution is $C_{dyn}\, k^2 \partial_t P_{\mathbf{k}}(t)$ (Methods):

$$\partial_t P_{\mathbf{k}}(t) = -\left[Dk^2 + C_{dyn}\, k^2 \partial_t + \cdots\right] P_{\mathbf{k}}(t), \tag{4}$$

where $P_{\mathbf{k}}(t)$ is the Fourier component of the polarization with wavevector $\mathbf{k}$. This term induces two striking modifications to the diffusive dynamics. First, the early time polarization profile follows a Yukawa form, $\frac{1}{r}e^{-r/\ell}$, and only crosses over to a Gaussian at late times (Methods). Second, the relationship between the height of the polarization profile $S_p(t)$, and its width, given by $\sqrt{Dt}$, is fundamentally altered; more precisely, to faithfully extract D from $S_p(t)$, one must account for the non-Gaussianity of the polarization profile.

To connect our nanoscale spin dynamics to these disorder-induced hydrodynamical features, we utilize a semiclassical description of the polarization evolution based on Fermi's golden rule (Fig. 1c, Methods). Accounting for both positional disorder and on-site random fields, numerical simulations of the polarization dynamics exhibit excellent agreement with the experimentally measured $S_p(t)$ for over three decades in time (Fig. 1b). Our semiclassical model also provides direct access to the spatial polarization profile, which remains robustly non-Gaussian throughout the timescale of the experiment, indicative of unconventional diffusion. Remarkably, the polarization profile precisely exhibits the predicted Yukawa-to-Gaussian crossover (Fig. 1d) and enables us to extract the coefficient of the dynamical modification (equation (4)) as $C_{dyn} = 204 \pm 45$ nm^2. A few remarks are in order. First, this coefficient defines a physical length scale, $\ell = \sqrt{C_{dyn}} = 14.3 \pm 1.6$ nm, which sets the decay of the Yukawa form, $\frac{1}{r}e^{-r/\ell}$, of the polarization profile. More intuitively, ℓ can be thought of as the length scale over which the disorder-induced variations of the local P1 environments start to become averaged out. Thus, only when the polarization expands to a characteristic size much larger than ℓ, will the dynamics approach Gaussian diffusion.

Second, as evinced in Fig. 1d, for a wide range of intermediate timescales, the polarization profile is well described by a simple exponential, which modifies the relationship between the survival probability and the diffusion coefficient. This modification can be computed analytically and takes the form of a geometric factor $g = 2\pi^{1/3}$, wherein $D \to gD$ (Table 1, Methods). Crucially, the mean squared displacement of the polarization profile, $\langle r^2\rangle(t) = 6D_{\langle r^2\rangle}t$, provides an independent measure of the diffusion coefficient[42,43]. As highlighted in Table 1, only by accounting for the disorder-induced geometric factor do we observe agreement between the diffusion coefficient extracted from $S_p(t)$ and $\langle r^2\rangle(t)$; this agreement directly demonstrates the non-Gaussian nature of the observed dynamics.

Microscopic control of emergent spin diffusion

We now demonstrate the ability to directly translate changes in the underlying microscopic Hamiltonian to changes in the emergent macroscopic behaviour. To engineer the Hamiltonian, we exploit the hyperfine structure of the P1 defect, enabling control over the effective density and the on-site random field disorder. In particular, sweeping the strength of the external magnetic field from 490 G to 540 G reveals five spectroscopically distinct subgroups of the P1 ensemble[36,37], each containing a different fraction of the total P1 spins, with density ratios $\nu = \{1/12, 1/4, 1/3, 1/4, 1/12\}$ (Fig. 3a, Supplementary Information). Thus, tuning the external magnetic

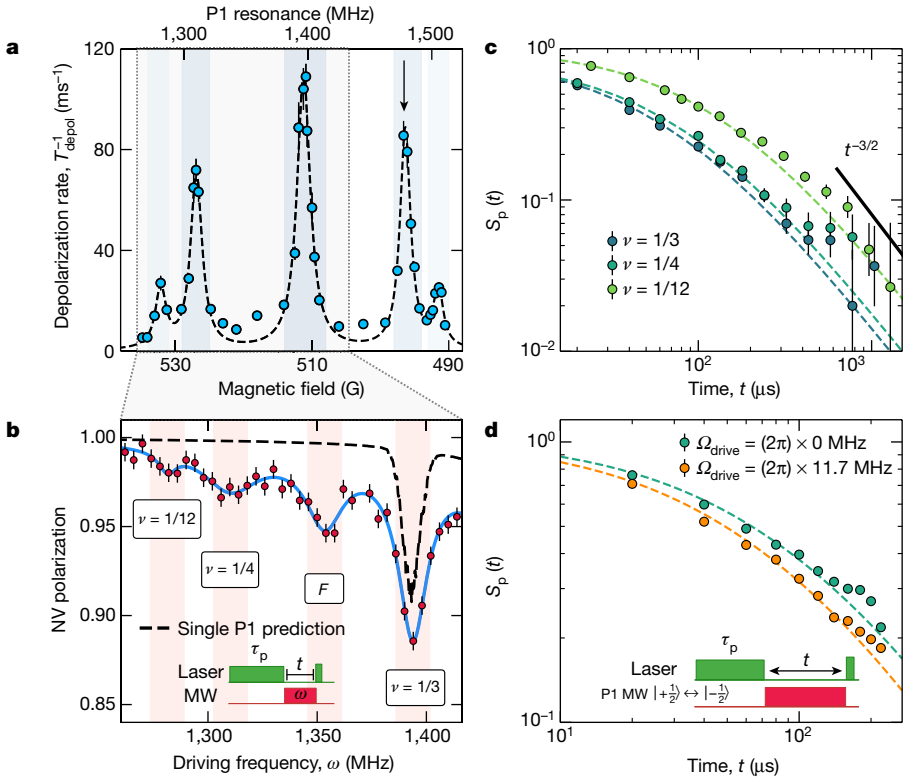

Fig. 3 | Controlling emergent hydrodynamics by engineering the microscopic Hamiltonian. a, Depolarization rate, $T_{1,\mathrm{depol}}^{-1}$, of the NV centre as a function of magnetic field after $\tau_p = 1$ μs. The NV exhibits five distinct resonances (blue shaded regions) corresponding to five different subgroups of P1s with density ratios $\nu \in \{1/12, 1/4, 1/3, 1/4, 1/12\}$. For panels **b**, **d** below, we fix the magnetic field strength, $B = 496.5$ G, wherein the NV is resonant with a $\nu = 1/4$ P1 subgroup (indicated by the arrow); the top axis shows the frequency of the P1 subgroups at this field strength. **b**, Fixing a polarization time, $\tau_p = 300$ μs, and an interaction time $t = 3$ μs (inset), we probe the polarization transfer between the NV and the resonant $\nu = 1/4$ P1 subgroup. By driving the other P1 subgroups, one can effectively reduce the magnitude of the on-site disorder by 'echoing' out a portion of the Ising piece of the dipolar interactions. Sweeping the microwave driving frequency, ω, we observe an enhanced NV decay (red dots with blue guide to the eye) when it is resonant with the $\nu = 1/12$, $\nu = 1/4$ and $\nu = 1/3$ subgroups as well as an additional 'forbidden' transition, F (Supplementary Information). By comparing against numerical simulations for a single P1 spin (dashed black line), we conclude that—aside from the $\nu = 1/3$ resonance where an additional hyperfine depolarization channel plays a crucial role—echoing out disorder enhances the coherent many-body interactions and leads to faster dynamics. **c**, Dynamics of $S_p(t)$ for different effective P1 densities with $\tau_p = 100$ μs; control over the P1 density is achieved by tuning the external magnetic field to bring the NV into resonance with the $\nu = 1/3$, $\nu = 1/4$ and $\nu = 1/12$ P1 subgroups. A smaller P1 density leads to correspondingly slower spin diffusion (Table 1). **d**, Dynamics of $S_p(t)$ for different on-site disorder strengths with $\tau_p = 300$ μs. Under continuous microwave driving ($\Omega_{\mathrm{drive}} = (2\pi) \times 11.7$ MHz) of the other $\nu = 1/4$ P1 subgroup (inset), the effective disorder is suppressed and spin diffusion is enhanced (Table 1). Dashed lines in **c**, **d** correspond to $S_p(t)$ obtained via equation (3). All experimental data are taken using sample S1 at room temperature $T \approx 300$ K. Errors represent 1 s.d. accounting statistical uncertainties.

field provides discrete control over the average spacing between resonant P1 spins. As shown in Fig. 3c, the survival probability for both the $\nu = 1/4$ and $\nu = 1/12$ P1 subgroups exhibits much slower spin diffusion than the $\nu = 1/3$ subgroup. This is consistent with the presence of weaker interactions arising from the larger spin spacing, and leads to smaller values for the measured diffusion coefficient (Table 1).

Finally, one can also experimentally control the strength of the on-site random field disorder via continuous driving. As these fields are dominated by the Ising portion of the interactions between the various P1 subgroups, rapid microwave driving of a single subgroup causes its contributions to the disorder to become averaged out (Fig. 3b). Indeed, by bringing the NV into resonance with one of the $\nu = 1/4$ subgroups (black arrow, Fig. 3a), while driving the other $\nu = 1/4$ subgroup, we observe faster spin diffusion, consistent with a reduction in disorder (Fig. 3d, Table 1).

Outlook

Looking forward, our work opens the door to a number of intriguing future directions. First, the presence of long-range, power-law interactions can lead to different dynamical universality classes[44]. Within our semiclassical model, the polarization dynamics are governed by an effective roughly $1/r^6$ power law (equation (11) in Methods). Interestingly, much like disorder, this particular power law also leads to an unconventional approach to diffusion, albeit governed by a distinct non-analytic correction $C_{\mathrm{lr}} k^3$ (Methods); our data (Fig. 1b, inset) do not exhibit clear signatures of this power-law correction and we leave its observation to future work. Second, the ability to experimentally isolate local equilibration dynamics naturally points to the study of many-body localization and Floquet thermalization[45,46]. In long-range interacting systems, the precise criteria for delocalization remain unknown[47,48], whereas in Floquet systems, the late-time dynamics involve a complex interplay between heating and hydrodynamic behaviour[11,49]. Finally, the presence of a Yukawa polarization profile in our system is reminiscent of an open question in the biochemical sciences, namely, what is the underlying mechanism behind the widespread emergence of Fickian yet non-Gaussian diffusion in complex fluids[15–20]; in such systems, it is notoriously difficult to change the microscopic equations of motion, suggesting the possibility for our platform to be utilized as a controllable 'simulator' of soft, heterogeneous materials. A direct route for exploring this question is to leverage subdiffraction imaging techniques or magnetic field gradients to measure correlation functions between spatially separated NVs[50,51].

Online content

Any methods, additional references, Nature Research reporting summaries, source data, extended data, supplementary information, acknowledgements, peer review information; details of author contributions and competing interests; and statements of data and code availability are available at https://doi.org/10.1038/s41586-021-03763-1.

1. Ljubotina, M., Žnidarič, M. & Prosen, T. Spin diffusion from an inhomogeneous quench in an integrable system. *Nat. Commun.* **8**, 16117 (2017).
2. Sommer, A., Ku, M., Roati, G. & Zwierlein, M. W. Universal spin transport in a strongly interacting Fermi gas. *Nature* **472**, 201–204 (2011).
3. Moll, P. J., Kushwaha, P., Nandi, N., Schmidt, B. & Mackenzie, A. P. Evidence for hydrodynamic electron flow in $PdCoO_2$. *Science* **351**, 1061–1064 (2016).
4. Bandurin, D. et al. Negative local resistance caused by viscous electron backflow in graphene. *Science* **351**, 1055–1058 (2016).
5. Crossno, J. et al. Observation of the dirac fluid and the breakdown of the Wiedemann–Franz law in graphene. *Science* **351**, 1058–1061 (2016).
6. Cepellotti, A. et al. Phonon hydrodynamics in two-dimensional materials. *Nat. Commun.* **6**, 6400 (2015).
7. Castro-Alvaredo, O. A., Doyon, B. & Yoshimura, T. Emergent hydrodynamics in integrable quantum systems out of equilibrium. *Phys. Rev. X* **6**, 041065 (2016).
8. Andreev, A., Kivelson, S. A. & Spivak, B. Hydrodynamic description of transport in strongly correlated electron systems. *Phys. Rev. Lett.* **106**, 256804 (2011).
9. Bertini, B., Collura, M., De Nardis, J. & Fagotti, M. Transport in out-of-equilibrium *XXZ* chains: exact profiles of charges and currents. *Phys. Rev. Lett.* **117**, 207201 (2016).
10. Bulchandani, V. B., Vasseur, R., Karrasch, C. & Moore, J. E. Solvable hydrodynamics of quantum integrable systems. *Phys. Rev. Lett.* **119**, 220604 (2017).
11. Ye, B., Machado, F., White, C. D., Mong, R. S. & Yao, N. Y. Emergent hydrodynamics in nonequilibrium quantum systems. *Phys. Rev. Lett.* **125**, 030601 (2020).
12. De Nardis, J., Bernard, D. & Doyon, B. Hydrodynamic diffusion in integrable systems. *Phys. Rev. Lett.* **121**, 160603 (2018).
13. Bertini, B. et al. Finite-temperature transport in one-dimensional quantum lattice models. *Rev. Mod. Phys.* **93**, 025003 (2021).
14. Ku, M. J. et al. Imaging viscous flow of the Dirac fluid in graphene. *Nature* **583**, 537–541 (2020).
15. Chechkin, A. V., Seno, F., Metzler, R. & Sokolov, I. M. Brownian yet non-Gaussian diffusion: from superstatistics to subordination of diffusing diffusivities. *Phys. Rev. X* **7**, 021002 (2017).
16. Stylianidou, S., Kuwada, N. J. & Wiggins, P. A. Cytoplasmic dynamics reveals two modes of nucleoid-dependent mobility. *Biophys. J.* **107**, 2684–2692 (2014).
17. Kim, J., Kim, C. & Sung, B. J. Simulation study of seemingly Fickian but heterogeneous dynamics of two dimensional colloids. *Phys. Rev. Lett.* **110**, 047801 (2013).
18. Chubynsky, M. V. & Slater, G. W. Diffusing diffusivity: a model for anomalous, yet brownian, diffusion. *Phys. Rev. Lett.* **113**, 098302 (2014).
19. Postnikov, E. B., Chechkin, A. & Sokolov, I. M. Brownian yet non-Gaussian diffusion in heterogeneous media: from superstatistics to homogenization. *New J. Phys.* **22**, 063046 (2020).
20. Barkai, E. & Burov, S. Packets of diffusing particles exhibit universal exponential tails. *Phys. Rev. Lett.* **124**, 060603 (2020).
21. Wurtz, J. & Polkovnikov, A. Quantum hydrodynamics in spin chains with phase space methods. *Phys. Rev. E* **101**, 052120 (2020).
22. Khemani, V., Vishwanath, A. & Huse, D. A. Operator spreading and the emergence of dissipative hydrodynamics under unitary evolution with conservation laws. *Phys. Rev. X* **8**, 031057 (2018).
23. Levstein, P., Pastawski, H. & Calvo, R. Spin diffusion in low-dimensional copper-amino-acid complexes. *J. Phys. Condens. Matter* **3**, 1877–1888 (1991).
24. Narozhny, B., Gornyi, I., Titov, M., Schütt, M. & Mirlin, A. Hydrodynamics in graphene: linear-response transport. *Phys. Rev. B* **91**, 035414 (2015).
25. Moore, G. D. & Sohrabi, K. A. Kubo formulas for second-order hydrodynamic coefficients. *Phys. Rev. Lett.* **106**, 122302 (2011).
26. Friedman, A. J., Gopalakrishnan, S. & Vasseur, R. Diffusive hydrodynamics from integrability breaking. *Phys. Rev. B* **101**, 180302 (2020).
27. Schemmer, M., Bouchoule, I., Doyon, B. & Dubail, J. Generalized hydrodynamics on an atom chip. *Phys. Rev. Lett.* **122**, 090601 (2019).
28. Zhang, W. & Cory, D. First direct measurement of the spin diffusion rate in a homogenous solid. *Phys. Rev. Lett.* **80**, 1324–1327 (1998).
29. Pagliero, D. et al. Optically pumped spin polarization as a probe of many-body thermalization. *Sci. Adv.* **6**, eaaz6986 (2020).
30. Boutis, G., Greenbaum, D., Cho, H., Cory, D. & Ramanathan, C. Spin diffusion of correlated two-spin states in a dielectric crystal. *Phys. Rev. Lett.* **92**, 137201 (2004).
31. Eberhardt, K. W., Mouaziz, S., Boero, G., Brugger, J. & Meier, B. H. Direct observation of nuclear spin diffusion in real space. *Phys. Rev. Lett.* **99**, 227603 (2007).
32. Kardar, M., Parisi, G. & Zhang, Y.-C. Dynamic scaling of growing interfaces. *Phys. Rev. Lett.* **56**, 889–892 (1986).
33. Žnidarič, M., Scardicchio, A. & Varma, V. K. Diffusive and subdiffusive spin transport in the ergodic phase of a many-body localizable system. *Phys. Rev. Lett.* **117**, 040601 (2016).
34. Gopalakrishnan, S. & Vasseur, R. Kinetic theory of spin diffusion and superdiffusion in *XXZ* spin chains. *Phys. Rev. Lett.* **122**, 127202 (2019).
35. Sinai, Y. G. The limiting behavior of a one-dimensional random walk in a random medium. *Theory Probab. Appl.* **27**, 256–268 (1983).
36. Doherty, M. W. et al. The nitrogen-vacancy colour centre in diamond. *Phys. Rep.* **528**, 1–45 (2013).
37. Hall, L. et al. Detection of nanoscale electron spin resonance spectra demonstrated using nitrogen-vacancy centre probes in diamond. *Nat. Commun.* **7**, 10211 (2016).
38. Khutsishvili, G. Spin diffusion and magnetic relaxation of nuclei. *Soviet Phys. JETP* **15**, (1962).
39. Takahashi, S., Hanson, R., Van Tol, J., Sherwin, M. S. & Awschalom, D. D. Quenching spin decoherence in diamond through spin bath polarization. *Phys. Rev. Lett.* **101**, 047601 (2008).
40. Hunt, G. A. Some theorems concerning brownian motion. *Trans. Am. Math. Soc.* **81**, 294–319 (1956).
41. Jarmola, A., Acosta, V., Jensen, K., Chemerisov, S. & Budker, D. Temperature-and magnetic-field-dependent longitudinal spin relaxation in nitrogen-vacancy ensembles in diamond. *Phys. Rev. Lett.* **108**, 197601 (2012).
42. Spitzer, F. *Principles of Random Walk* Vol. 34 (Springer Science & Business Media, 2013).
43. Einstein, A. *Investigations on the Theory of the Brownian Movement* (Courier Corporation, 1956).
44. Lévy, P. *Théorie de l'Addition des Variables Aléatoires* Vol. 1 (Gauthier-Villars, 1954).
45. Abanin, D. A., Altman, E., Bloch, I. & Serbyn, M. Colloquium: many-body localization, thermalization, and entanglement. *Rev. Mod. Phys.* **91**, 021001 (2019).
46. Mori, T., Ikeda, T. N., Kaminishi, E. & Ueda, M. Thermalization and prethermalization in isolated quantum systems: a theoretical overview. *J. Phys. B* **51**, 112001 (2018).
47. Yao, N. Y. et al. Many-body localization in dipolar systems. *Phys. Rev. Lett.* **113**, 243002 (2014).
48. Nandkishore, R. M. & Sondhi, S. L. Many-body localization with long-range interactions. *Phys. Rev. X* **7**, 041021 (2017).
49. Peng, P., Yin, C., Huang, X., Ramanathan, C. & Cappellaro, P. Observation of floquet prethermalization in dipolar spin chains. *Nature Physics* **17**, 444–447 (2021).
50. Rittweger, E., Han, K. Y., Irvine, S. E., Eggeling, C. & Hell, S. W. STED microscopy reveals crystal colour centres with nanometric resolution. *Nat. Photon.* **3**, 144–147 (2009).
51. Arai, K. et al. Fourier magnetic imaging with nanoscale resolution and compressed sensing speed-up using electronic spins in diamond. *Nat. Nanotechnol.* **10**, 859–864 (2015).

Methods

Coherence measurement of the P1 ensemble

To directly measure the coherent properties of P1 system, we first apply a laser pulse with duration $\tau_p = 1{,}000\ \mu s$ to polarize the $\nu = 1/3$ P1 subgroup, and then shelve the NV spin into the highly off-resonant $|+1\rangle$ sublevel for a fixed time $\tau_w = 30\ \mu s$ (Extended Data Fig. 1). Within this shelving period, we apply various dynamical decoupling sequences (Ramsey, XY-8 and interaction decoupling) to measure the P1 spin-coherence time T_2. Although the XY-8 is designed to cancel the Ising portion of the Hamiltonian, we implement a recently introduced robust interaction decoupling sequence (termed DROID-60) that decouples the full dipolar interaction[52,53]. After unshelving the NV spin back to $|0\rangle$, we wait for $\tau_0 = 10\ \mu s \approx \tau_{th}$ to let it locally thermalize with the nearby P1 spins, and detect the resulting NV polarization as a measure of local P1 polarization.

Crucially, as shown in Fig. 2e, when the dipolar interaction is fully cancelled, we observe a substantial enhancement of T_2, demonstrating that the spin dynamics are dominated by coherent interactions. In principle, such techniques can be employed to directly control the interaction strength between P1 spins, and thus provide a powerful tool for studying how the interaction strength affects the resulting transport dynamics. Unfortunately, it is technically challenging to utilize such pulse sequences to study long-time diffusive dynamics. The reason is the inevitable existence of pulse errors in the microwave control system. In particular, pulse errors can lead to two effects: (1) the cancellation of dipolar interactions is no longer perfect and (2) total magnetization is no longer conserved, thus leading to additional overall decay of the polarization.

In our experiment, to effectively decouple the P1–P1 dipolar interactions, one needs the pulse spacing to be much smaller than the typical interaction timescale $1/J$. As a result, to study hydrodynamics at late times, one needs to apply more than 10^4 pulses. With such a large number of pulses, even very small pulse imperfections could lead to an accumulated errors that affect the diffusive dynamics substantially. Tackling such issue requires a careful engineering of the microwave delivery system to enable the delivery of precise, homogeneous pulses. We hope to further explore this direction in future work.

Continuous diffusive model

To verify and study the late-time hydrodynamics of the system, we build up a phenomenological diffusion equation for the polarization profile. By solving this equation, we derive the functional form of the survival probability measured in our experiment. This allows us to extract the diffusion coefficient, as well as to study the subleading correction to diffusion in our disordered long-range interacting system.

Gaussian diffusion and associated survival probability. In a diffusive system, the polarization dynamics should be, at leading order, captured by the following diffusion equation:

$$\partial_t P(t,\mathbf{r}) = D\nabla^2 P(t,\mathbf{r}) - \frac{P(t,\mathbf{r})}{T_1} + Q(t,\mathbf{r}), \tag{5}$$

where $P(t,\mathbf{r})$ is the polarization as a function of both time t and position $\mathbf{r}$, D is the diffusion coefficient, T_1 is the intrinsic depolarization timescale of our system and $Q(t,\mathbf{r})$ corresponds to the polarization source (the NV). Considering our experimental geometry and polarization protocol, we assume that the polarization process occurs over a short distance b while the laser is on and can be modelled by:

$$Q(t,\mathbf{r}) = \begin{cases} \dfrac{\Gamma}{(2\pi b^2)^{3/2}} e^{-r^2/(2b^2)} & -\tau_p < t < 0 \\ 0 & t > 0 \end{cases}, \tag{6}$$

where Γ is the polarization rate. The presense of a finite b reflects the range of the polarization transfer process from the NV to the P1 ensemble and guarantees that the polarization does not diverge at short times.

This problem can be solved via a Green's function formalism (Supplementary Information), which yields the solution:

$$P(t,\mathbf{r}=0) = \frac{\Gamma e^{\frac{b^2}{DT_1}}}{4\pi D^{\frac{3}{2}}\sqrt{T_1}} \times \left\{ F\left[\left(t+\frac{b^2}{D}\right)/T_1\right] - F\left[\left(t+\tau_p+\frac{b^2}{D}\right)/T_1\right]\right\}, \tag{7}$$

where the function $F(x)$ is defined as

$$F(x) = \frac{1}{\sqrt{\pi}}\frac{e^{-x}}{\sqrt{x}} - \mathrm{erfc}(\sqrt{x}). \tag{8}$$

In Fig. 3b, d, we also consider the situation where an off-resonant P1 subgroup is driven with a microwave field to 'cancel' the Ising interaction and thus reduce the on-site field strength. This leads to a faster diffusion with coefficient D^{dr}.

To capture the hydrodynamics in this setup, we must incorporate this diffusion coefficient in equation (5) after the polarization process ($t \geq 0$)—throughout polarization the system remains undriven and the diffusion coefficient is D. We also note that the decay timescale (denoted as T_1^{dr}) may also get modified. Following the similar approach to analyse the undriven case (Supplementary Information), we obtain the survival probability for the experiment as

$$\begin{aligned} &P(t,\mathbf{r}=0) \\ &= \frac{\Gamma e^{\frac{b^2}{DT_1}}}{4\pi D^{3/2}\sqrt{T_1}} e^{\left(\frac{D^{dr}}{D}-\frac{T_1}{T_1^{dr}}\right)\frac{t}{T_1}} \times \left\{ F\left[\left(\frac{D^{dr}}{D}t+\frac{b^2}{D}\right)/T_1\right]\right. \\ &\left. - e^{\left(\frac{T_1^{dr}}{T_1}-\frac{D}{D^{dr}}\right)\frac{\tau_p}{T_1^{dr}}} F\left[\left(\frac{D^{dr}}{D}t+\tau_p+\frac{b^2}{D}\right)/T_1\right]\right\}. \end{aligned} \tag{9}$$

Details of fitting with diffusion equation. Up until now, we have been considering the dynamics of a single NV centre surrounded by an ensemble of P1 spins. However, the finite NV defect density ρ_{NV} in our sample leads to the polarization overlap between different NV–P1 systems. Owing to the randomness in the NV centre positions, this effect can be captured by a simple constant background. In particular, as each NV is randomly placed in the system and we measure all NVs, the above overlap effect is spatially averaged and can be treated as a homogeneous background whose dynamics is governed only by depolarization. Given the volume of each NV–P1 system, $V = 1/\rho_{NV}$, the background polarization is simply written as:

$$P_{bg}(t) = \frac{1}{V}\int_{-\tau_p}^{0} \Gamma e^{-(t-t_0)/T_1} dt_0 = \rho_{NV}\Gamma T_1 (e^{-t/T_1} - e^{-(t+\tau_p)/T_1}). \tag{10}$$

Combining the background polarization P_{bg} with the survival probability $P(t,\mathbf{r}=0)$ (that is, equations (7) and (9)) yields the experimental signal, from where we extract the diffusion coefficient D and the range of polarization b (using an independently calibrated T_1; Extended Data Fig. 3). To be specific, for the sample S1 at room temperature and for each ν, we fit to a global value of D and b, while letting Γ change across different τ_p (Extended Data Fig. 2). In the driven experiment, we use the values of b, Γ, D and T_1 from the undriven case, as well an independently calibrated T_1^{dr} (see below) to fit the data and extract D^{dr} as the sole fitting parameter (Fig. 3d). For the sample S2 at low temperature (which has a similar P1 density to sample S1) fit to D, Γ and b with T_1 being independently characterized from the late-time decay (grey curve in Fig. 1b). Here, we emphasize that in the fitting functional form,

ρ_{NV} (which is independently measured; Supplementary Information) provides the necessary length scale that connects the measured decay timescales to the diffusion coefficient.

Extraction of late-time T_1 time. One important parameter in extracting the dynamics of the survival probability $S_p(t)$ from the observed NV dynamics is the extrinsic polarization time T_1 of the P1 centres. This depolarization timescale can have multiple contributions (for example, phonon depolarization, Jahn–Teller instability and interactions with other off-resonant spins[39]) and is, thus, highly dependent on the details of the experiment, such as temperature, defect density and application of additional driven fields. To this end, we extract it via the late-time behaviour of the polarization dynamics under different conditions; at late time, the local polarization profile has expanded and the observed dynamics is dominated by the slowly decay of the background polarization (Extended Data Fig. 3).

Derivation of geometric factor correction to diffusion

Although both Gaussian and exponential (Fig. 1) polarization profiles exhibit the same diffusive scaling for the survival probabilities, the difference in their shapes modifies the relationship between the height and the width of the distribution and thus how one can extract the diffusion coefficient. In particular, in the Gaussian case this relationship is given by $S_p^g(t) = P_{tot}/(2\pi\langle r^2\rangle)^{3/2}$ whereas in the exponential case it is given by $S_p^e(t) = P_{tot}/[8\pi(\langle r^2\rangle)^{3/2}]$, where P_{tot} is the total polarization in the system. Replacing with $\langle r^2\rangle = 6Dt$ and equating the two survival probabilities leads to a constant factor correction $g = 2\pi^{1/3}$ between the two diffusion coefficients. As such, the extracted diffusion coefficients (extracted assuming a Gaussian profile), should be corrected by multiplying its value by g. Crucially, the corrected diffusion coefficients are in excellent agreement with the diffusion coefficients directly extracted via the growth of the mean squared displacement $\langle r^2\rangle$.

Semiclassical model

Although the precise many-body quantum dynamics of our model are dictated by the underlying microscopic Hamiltonian, its calculation remains beyond the realm of possibility of current numerical techniques. To this end, we build a semiclassical model of the polarization dynamics based on the the microscopic details of the Hamiltonian that allows us to quantitatively characterize the observed dynamics (for example, extracting the diffusion coefficient), as well as investigate properties beyond the current experimental reach (for example, studying the spatial profile of the polarization). Crucially, this model provides a direct and quantitative connection between the underlying microscopic Hamiltonian and the emergent macroscopic dynamics.

At its core, our approach relies on the calculation of the polarization-transfer rate, Γ_{ij}, between any pair of P1 spins via Fermi's golden rule (Fig. 1c):

$$\Gamma_{ij} = \left(\frac{J_0\widetilde{A}_{i,j}}{r_{ij}^3}\right)^2 \frac{2\gamma}{\gamma^2 + (\delta_i - \delta_j)^2}. \tag{11}$$

Each of the relevant parameters is independently measured: $\gamma \approx 0.5\ \mu s^{-1}$ represents the interaction-induced linewidth and is characterized by the spin-echo decoherence time of the NV centre; δ_i represents the strength of the on-site random fields and is drawn from a distribution with width $W \approx (2\pi) \times 4.5$ MHz, characterized by the NV linewidth (Extended Data Fig. 4). The analogous polarization transfer rate between NV and P1 spins is obtained by replacing $\widetilde{A}_{i,j}$ with A_i. For details of the derivation, see Supplementary Information.

Armed with the rate of polarization transfer, we numerically study the polarization dynamics of the system by reducing the exponentially large quantum state of the system (2^N coefficients for N spins), into $2N$ coefficients that capture the individual populations $\rho_{i,\sigma}$ of each of the levels σ of each spin i of the system. For P1, $\sigma \in \left\{-\frac{1}{2}, +\frac{1}{2}\right\}$, whereas for NV, $\sigma \in \{0, -1\}$. One then obtains a differential equation for the populations:

$$\partial_t \rho_{i,\sigma} = \sum_j \Gamma_{i,j}(\rho_{i,\bar{\sigma}}\rho_{j,\sigma'} - \rho_{i,\sigma}\rho_{j,\bar{\sigma'}}), \tag{12}$$

where $\bar{\sigma}$ corresponds to the other level of the spin i and σ' corresponds to the level of spin j such that interactions lead to a transition $\sigma\bar{\sigma'} \leftrightarrow \bar{\sigma}\sigma'$.

To simulate the spin-polarization process, we further extend the differential equations to include the remaining ground and excited states of the NV centre (Supplementary Information). Accounting for both positional disorder and on-site random fields, numerical simulations of the polarization dynamics exhibit excellent agreement with the experimentally measured $S_p(t)$ (Extended Data Fig. 5).

Computing the diffusion coefficient from the semiclassical description

One of the features of our semiclassical model is the ability to access the spatial profile of the polarization, enabling an independent characterization of the diffusive dynamics via the direct study of the spread of the entire polarization profile. In particular, we leverage our semiclassical model to compute the mean squared displacement of the polarization and observe the characteristic linear growth with time (Extended Data Fig. 6). From this linear growth, we can directly extract the diffusion coefficient of the dynamics via

$$\langle r^2\rangle = 6D_{\langle r^2\rangle}t, \tag{13}$$

where the coefficient $6 = 2d$ includes the information about the dimensionality d of our system.

Focusing our analysis on the dynamics of the P1 centres, we can disregard the details of the NV and transform our semiclassical model into a set of linear differential equations on the polarization of the P1 centres $P_i = \rho_{i,\uparrow} - \rho_{j,\downarrow}$:

$$\dot{P}_i = \sum_j \Gamma_{ij}\left(P_j - P_i\right) \tag{14}$$

Crucially, this linearity condition enables us to map this set of differential equations into a continuous-time random walk of the polarization through the positions of the defects. Such an approach enables us to consider the polarization dynamics of much larger system sizes (up to $N \approx 4 \times 10^4$ P1s) because we no longer need to build the dense transition rate matrix Γ_{ij} and solve for the associated eigenvalue problem.

Our simulation protocol is then as follows. We first generate an ensemble of P1 spins with random positions $\mathbf{r}_i$ and onsite energies δ_i surrounding a P1 spin at position $\mathbf{r}_0 = (0, 0, 0)$. Starting with the polarization at $\mathbf{r}_0$ at $t = 0$, we compute its dynamics through the system as follows. When the polarization is on spin i (at position $\mathbf{r}_i$), the hopping rate away from spin i is given by $\Gamma_{tot} = \sum_j \Gamma_{ij}$; thus the polarization remains in spin i for time δt which is a Poisson random variable with mean Γ_{tot}^{-1}. The probability of hopping to spin j is given by the branching ratio $\beta_j = \Gamma_{ij}/\Gamma_{tot}$. We repeat this process until a time $t_{max} \approx 1{,}000\ \mu s$ has elapsed.

Computing the mean squared displacement. For each random walk, we record the displacement squared of the polarization from its original position $\mathbf{r}_0$ as a function of time t. Averaging over many random walks immediately yields the mean squared displacement of the polarization profile.

Unfortunately, this quantity is particularly sensitive to the system size considered (which sets an upper bound on the maximal $\langle r^2\rangle(t)$), specially given the long-range nature of the transition rates (Extended

Data Fig. 6). To this end, we perform a finite size scaling, where we extrapolate the infinite system size behaviour by studying $\langle r^2\rangle(t)$ for different system sizes $N \in \{10^3, 15^3, 20^3\, 25^3, 30^3\}$ and assuming that the system-size effects are linear with the inverse lengthscale of the system $L^{-1} \approx N^{-1/3}$. We find that this ansatz agrees with the observed numerical data, and leads to a long-lived linear increase in the $\langle r^2\rangle(t)$, from which we can extract the diffusion coefficient in our semiclassical description. We estimate the error in our analysis by fitting equation (13) to different early time regimes (from 0 to $T_{max} \in [30, 300]$ μs) and taking its value as half the range of extracted diffusion coefficients.

Dynamical correction to diffusion

The experiments average over both NV centres within the sample and shot-to-shot fluctuations in the environment. Thus, the quantity of interest is the disorder-averaged diffusion kernel, or Green's function. In frequency and momentum space, this is given by:

$$G(\mathbf{k}, \omega) = \frac{1}{-i\omega + Dk^2 + \Sigma(\mathbf{k}, \omega)} \tag{15}$$

where $-i\omega + Dk^2$ describes the eventual diffusive dynamics at asymptotically late times (small frequencies ω) and long wavelengths (small wavevectors $\mathbf{k}$), and the self-energy $\sum(\mathbf{k}, \omega)$ captures the corrections due to disorder averaging. Focusing on the leading corrections in this limit, the small ω and $\mathbf{k}$ expansion of $\sum(\mathbf{k}, \omega)$ can be constrained by noting that it is (1) analytic, (2) isotropic and (3) probability conserving:

$$\Sigma(\mathbf{k}, \omega) = D'k^2 + Ck^4 + \ldots + (-i\omega)(\ell^2 k^2 + \ell'^4 k^4 + \ldots) + \ldots, \tag{16}$$

where $\ell^2 = C_{dyn}$ in the main text and C is the next leading order coefficient. Note that in the time domain, this self-energy directly leads to equation (4).

A few remarks are in order. First, the $D'k^2$ term simply corrects the bare diffusion coefficient, $D \to D + D'$, and can be absorbed into a new definition of D. Second, the Ck^4 and $\ell^2(-i\omega)k^2$ terms have the same scaling dimension near the diffusive fixed point (where $z = 2$); they are accordingly the leading irrelevant corrections in the renormalization group sense. Third, the dynamical corrections (involving powers of ω) do not appear in translationally invariant classical hopping systems, where the only corrections in $\sum$ arise due to the spatial Fourier transform of the hopping kernel. This picture is modified in disordered systems, where a diagrammatic analysis of the disorder average generically yields the dynamical corrections. Finally, although equation (16) follows on very general symmetry grounds, we can strictly derive the dynamical correction by computing the one-loop self-energy in a continuum model with a spatially random local diffusion coefficient (Supplementary Information).

We now tease out the phenomenological role of the dynamical correction term for the observed diffusion. Focusing on the short-range case (without $k^{\alpha-d}$ correction for long-range interacting systems with power-law exponent α):

$$G(\mathbf{k}, \omega) = \frac{1}{-i\omega\left(1 + \ell^2 k^2\right) + Dk^2} \Rightarrow G(\mathbf{k}, t) = \frac{e^{-Dk^2 t/\left(1+\ell^2 k^2\right)}}{1 + \ell^2 k^2}. \tag{17}$$

In the $t \to 0$ limit, the polarization profile approaches the Yukawa potential form $G(\mathbf{k}, t = 0) = \frac{1}{1+\ell^2 k^2}$ (ref. [54]). Returning to real space in three dimensions

$$G(\mathbf{r}, t = 0) = \frac{e^{-r/\ell}}{4\pi\ell^2 r}. \tag{18}$$

We note that this form should be interpreted as the shape to be expected of G at early times in the crossover to Gaussian behaviour. It does not reduce to a delta function because we have neglected the higher-order k and ω corrections that govern the short-distance, early-time dynamics.

However, the presence of this dynamical correction has important late-time effects as well. From equation (17), one observes that the large k modes now decay with a constant rate. This implies that the short-distance singularity of the Yukawa-potential decays only after the timescale ℓ^2/D.

We end this section with a few more remarks. First, at even later times, the weight of the singularity decays exponentially whereas the diffusive behaviour of the survival probability decays as a power law in time, $S_p(t) \approx t^{-d/2}$, dominating the late-time physics. This is in agreement with the presence of the late-time diffusive fixed point. Second, such a singularity cannot be experimentally observable owing to the short-range cutoff of our system: we measure the polarization of the NV centres, which must remain finite. One can understand this singularity as being regularized by the short-range details arising from the discrete nature of our randomly positioned spin system. Finally, while the $D'k^4$ term has the same scaling dimension as $(-i\omega)\ell^2 k^2$, its inclusion in the analysis above does not change the qualitative statements, nor does it alter the nature of the early time behaviour (it only appears in the exponent of equation (17) and does not change the $t \to 0$ behaviour).

Extracting dynamical correction C_{dyn}

To extract the strength of dynamical correction, we consider the same methodology when extracting the diffusion coefficient from the rate equation model, but instead of computing the mean squared displacement, we focus on the details of the polarization profile. From our analytical derivation, the dynamics of such polarization profile are dominated by a diffusive and a disorder-generated term at late enough times. The value of $C_{dyn} = \ell^2$ can be then obtained by fitting the resulting evolution to the dynamics under the diffusion correction (including the dynamical correction), starting from a Yukawa form for the polarization profile (Fig. 1). To minimize finite size and time biases, we consider the dynamics between t_{min} and t_{max}, the latter set to the time when the polarization per spin at the edge is larger than 3×10^{-6}. The reported value of ℓ corresponds to an average over the values extracted for different t_{min} over the range where the values are consistent (last three data points in Extended Data Fig. 7). We summarize the extracted ℓ in Extended Data Table 1.

Long-range modifications to diffusion

Although we leave the detailed derivation in the Supplementary Information, we summarize our conclusion on the long-range modification here. With the presence of long-range interaction, the decay rate of a $\mathbf{k}$-mode $f(\mathbf{k})$ in general can be written as:

$$f(\mathbf{k}) = Dk^2 + C_{lr}k^{\alpha-d} + Ck^4 + \cdots \tag{19}$$

where D, C_{lr} and C are model-dependent coefficients. This result immediately highlights three import regimes. When $d < \alpha < d + 2$, the leading power is no longer the k^2 term and instead a $k^{\alpha-d}$ term becomes the leading contribution—the system is no longer diffusive and enters the Lévy-flight regime[44,55]. When $d + 2 < \alpha < d + 4$, the leading order term remains the diffusive term but the subleading correction that control the approach to diffusion is set by a $k^{\alpha-d}$ term[56]. When $d + 4 < \alpha$, neither the leading term nor the subleading term arises from the long-range transfer rate and the dynamics do not deviate substantially from the short-range case.

We now emphasize that, in the window of intermediate power laws, $d + 2 < \alpha < d + 4$, the survival probability exhibits a qualitatively different approach ($\sim t^{-\alpha/2+1}$) to the diffusive fixed point. For the three-dimensional

systems that we focus on, at late times, the survival probability $P(\mathbf{r}=0,t)$ should follow:

$$P(t,\mathbf{r}=0)=\frac{1}{(4\pi Dt)^{3/2}}+\frac{C_{\mathrm{lr}}}{2\pi^2D^3t^2} \tag{20}$$

when $\alpha=6$ (our experimental platform), and

$$P(t,\mathbf{r}=0)=\frac{1}{(4\pi Dt)^{3/2}}+\frac{15C}{32\pi^{3/2}D^{7/2}t^{5/2}} \tag{21}$$

when $\alpha\geq 7$.

Clearly, the approximately t^{-2} approach is distinct from conventional diffusion where the approach is proportional to approximately $t^{-5/2}$ (Extended Data Fig. 8).

We also remark that, similar to a previous discussion, we should convolve the above survival probability with the polarization process (both polarization duration and short-range details) to obtain the correct form for our experimental signal.

Data availability

Source data are provided with this paper. Further data are available from the corresponding author upon reasonable request. Source data are provided with this paper.

52. Choi, J. et al. Robust dynamic hamiltonian engineering of many-body spin systems. *Phys. Rev. X* **10**, 031002 (2020).
53. Zhou, H. et al. Quantum metrology with strongly interacting spin systems. *Phys. Rev. X* **10**, 031003 (2020).
54. Yukawa, H. On the interaction of elementary particles. i. *Proc. Phys. Math. Soc. Jpn* **17**, 48–57 (1935).
55. Shlesinger, M. F., Zaslavsky, G. M. & Frisch, U. (eds) *Lévy Flights and Related Topics in Physics: Proc. of the International Workshop Held at Nice, France, 27–30 June 1994* (Lecture Notes in Physics, Springer-Verlag, 1995).
56. Schuckert, A., Lovas, I. & Knap, M. Nonlocal emergent hydrodynamics in a long-range quantum spin system. *Phys. Rev. B* **101**, 020416 (2020).
57. Bauch, E. et al. Decoherence of ensembles of nitrogen-vacancy centers in diamond. *Phys. Rev. B* **102**, 134210 (2020).
58. Mittiga, T. et al. Imaging the local charge environment of nitrogen-vacancy centers in diamond. *Phys. Rev. Lett.* **121**, 246402 (2018).

Acknowledgements We acknowledge the insights of and discussions with J. Choi, E. Davis, M. Dupont, D. Gangloff, S. Gopalakrishnan, A. Jayich, P. Stamp, R. Walsworth and H. Zhou. This work was supported as part of the Center for Novel Pathways to Quantum Coherence in Materials, an Energy Frontier Research Center funded by the US Department of Energy, Office of Science, Basic Energy Sciences under award number DE-AC02-05CH11231. A.J. acknowledges support from the Army Research Laboratory under Cooperative Agreement number W911NF-16-2-0008. S.H. acknowledges support from the National Science Foundation Graduate Research Fellowship under grant number DGE1752814. N.Y.Y. acknowledges support from the David and Lucile Packard foundation and the W. M. Keck foundation. The work of D.B. is supported by the EU FET-OPEN Flagship Project ASTERIQS (action 820394 and the Cluster of Excellence 'Precision Physics, Fundamental Interactions, and Structure of Matter' (PRISMA+ EXC 2118/1) funded by the German Research Foundation (DFG) within the German Excellence Strategy (project ID 39083149). C.R.L. acknowledges support from the NSF through PHY-1752727. S.C. acknowledges support from the Miller Institute for Basic Research in Science.

Author contributions C.Z., T.M., S.H. and P.B. performed the experiments. F.M., B.Y., S.C., B.K., C.R.L., J.E.M. and N.Y.Y. developed the theoretical models and methodology. C.Z., F.M., and B.Y. performed the data analysis. F.M. and B.Y. performed the numerical simulations. M.M., D.T., A.J. and D.B. prepared and provided the diamond substrates. C.R.L., J.E.M. and N.Y.Y. supervised the project. C.Z., F.M., B.Y., C.R.L., J.E.M. and N.Y.Y wrote the manuscript with input from all authors.

Competing interests The authors declare no competing interests.

Additional information

Supplementary information The online version contains supplementary material available at https://doi.org/10.1038/s41586-021-03763-1.

Correspondence and requests for materials should be addressed to N.Y.Y.

Peer review information *Nature* thanks Nir Bar-Gill, Benjamin Doyon and the other, anonymous, reviewer(s) for their contribution to the peer review of this work.

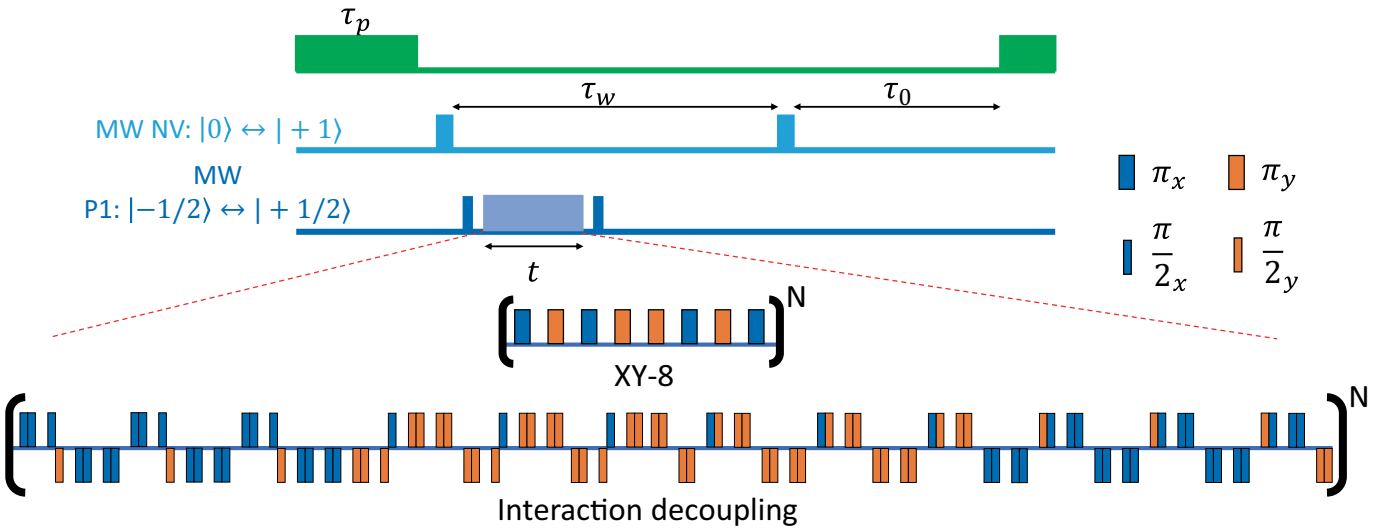

Extended Data Fig. 1 | Experimental sequence to measure the coherence of P1 ensemble. For XY-8 and interaction decoupling sequences, we fix the interval between pulses to be τ = 10 ns, and increase the number of repetition N. The P1 π(π/2) pulse duration is set to 36 ns (18 ns). In the interaction decoupling sequences, the pulses at bottom side correspond to rotations along $-\hat{x}$ (blue) and $-\hat{y}$ (orange) axes.

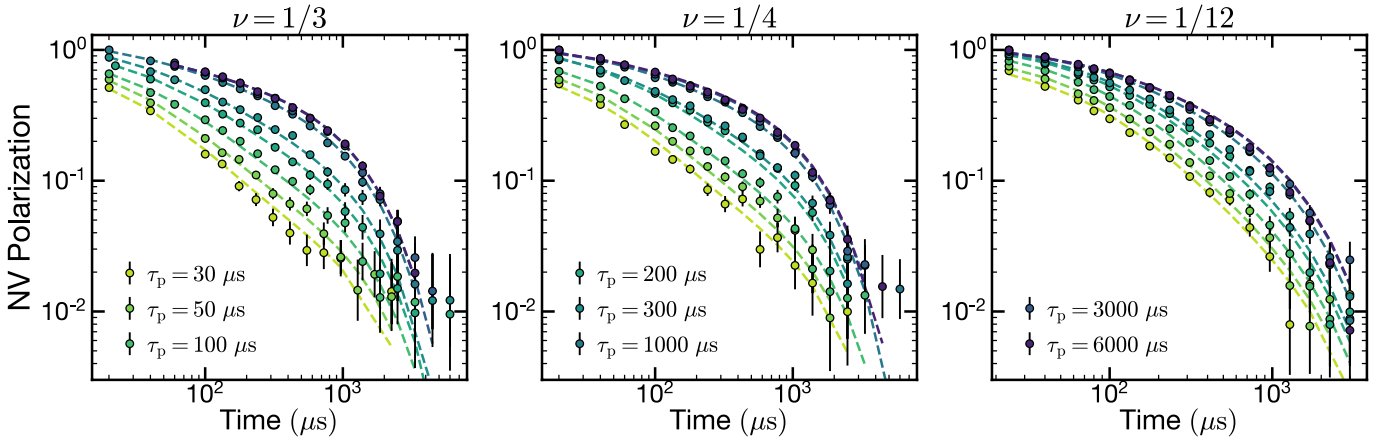

Extended Data Fig. 2 | Extraction of diffusion constants for sample S1. Fitting of the depolarization data in sample S1 for different groups ν (different panels) and different pumping times τ_p (different colours). For each group, we fit the experimental data across all τ_p data to a diffusive model in equation (7) with an additional background P_{bg}. From this procedure, we extract both D and b, as well as, a τ_p-dependent Γ, which captures the reduction in efficiency of the NV–P1 polarization transfer owing to the saturation of polarization near the NV.

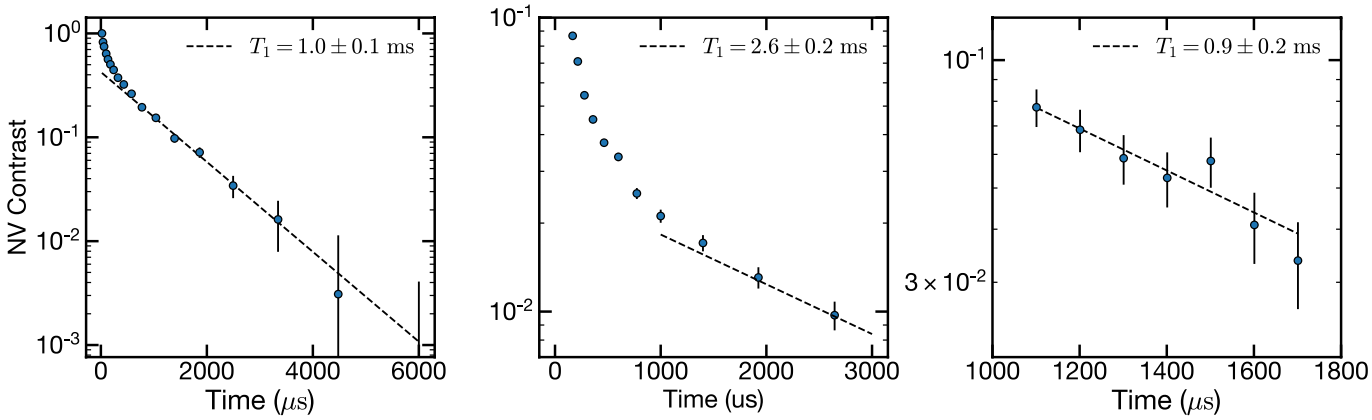

Extended Data Fig. 3 | Measurement of late time extrinsic decay time T_1 for different samples and under driving. a, **b**, Extraction of the extrinsic depolarization time of samples S1 and S2 at room and low temperature (25 K) and after polarizing for τ_p = 1,000 µs (**a**) and τ_p = 30 µs (**b**). The late time behaviour follows an exponential decay with timescale given by 1.0 ± 0.1 ms and 2.6 ± 0.2 ms, respectively. **c**, To extract the modified intrinsic depolarization time T_1^{dr} of v = 1/4 P1 subgroup with the presence of a strong microwave driving $\Omega = (2\pi) \times 11.7$ MHz on the other v = 1/4 subgroup, we apply the following pulse sequence: after a laser pumping time τ_p = 1000 µs, we wait for 1 ms so that the initial P1 spatial polarization profile diffuses to a nearly homogeneous background which decays with intrinsic depolarization time of P1 centres. We then turn on a continuous microwave driving on the other v = 1/4 P1 subgroup, and measure the resulting background decay; the resulting timescale is given T_1^{dr} = 0.9 ± 0.2 ms.

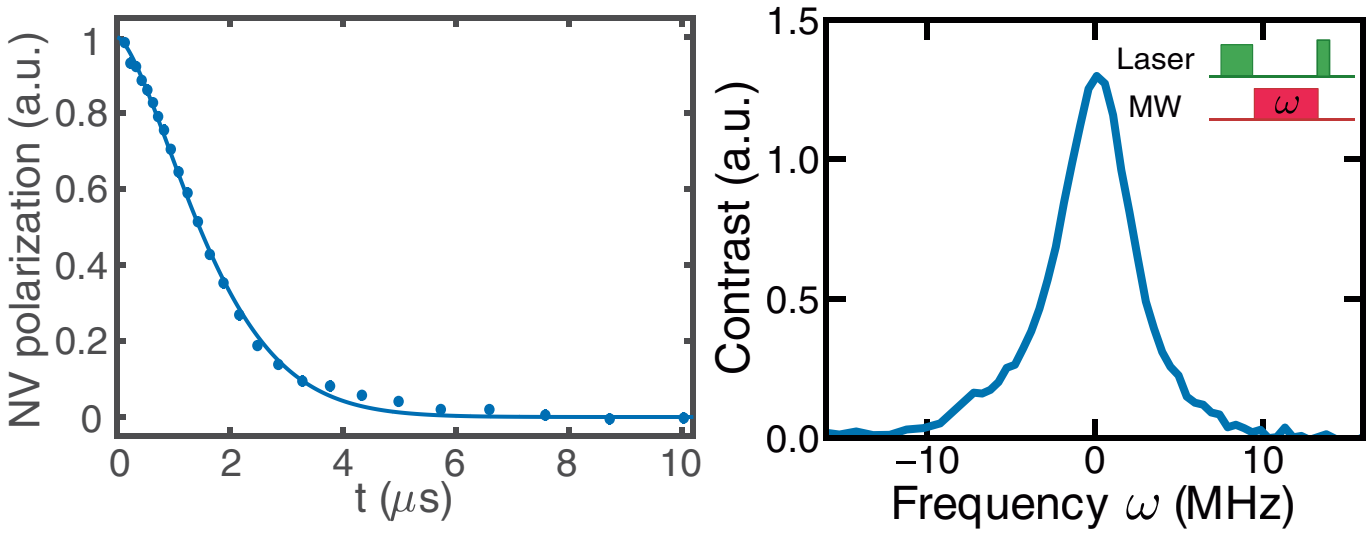

Extended Data Fig. 4 | Determination of the extrinsic decoherence rate γ and on-site random field distribution δ_i. a, We estimate the extrinsic decoherence rate γ in the rate equation using the measured spin-echo coherence time of the NV. After polarizing the NV centre via a green laser, a π/2 pulse prepares the NV spin into a coherent superposition of $|m_s = 0\rangle$ and $|m_s = -1\rangle$, which is allowed to dephase during a time t. A π pulse at the centre of the sequence 'echos' out the on-site random field generated by the nearby P1 centres, thus provides a direct estimation of the extrinsic decoherence time of a single spin in the system. We fit the spin-echo decay using a form $e^{-(t/T_2^{echo})^{1.5}}$ (ref. [57]) and extract $T_2^{echo} = 1.9 \pm 0.1\mu s$ ($\gamma \approx 1/T_2^{echo} \approx 0.5\mu s^{-1}$). **b**, The distribution of on-site random fields δ_i is directly determined using the intrinsic linewidth of the NV spin state. After polarizing the NV centre via a green laser, we apply a microwave π pulse and sweep its frequency ω across the NV $|0\rangle$ to $|-1\rangle$ transition. To avoid microwave power broadening of NV transition, we choose a sufficient weak microwave π pulse with duration 2 μs. Note that the measured linewidth is dominated by interactions with the dense P1 ensemble ($W \approx (2\pi) \times 4.5$ MHz) (Supplementary Information). The presence of nuclear ^{13}C spins leads to a much smaller contribution to the linewidth of about $(2\pi) \times 0.3$ MHz (ref. [58]). Crucially, both effects are taken into account in our analysis by sampling δ_i directly from the measured spectrum.

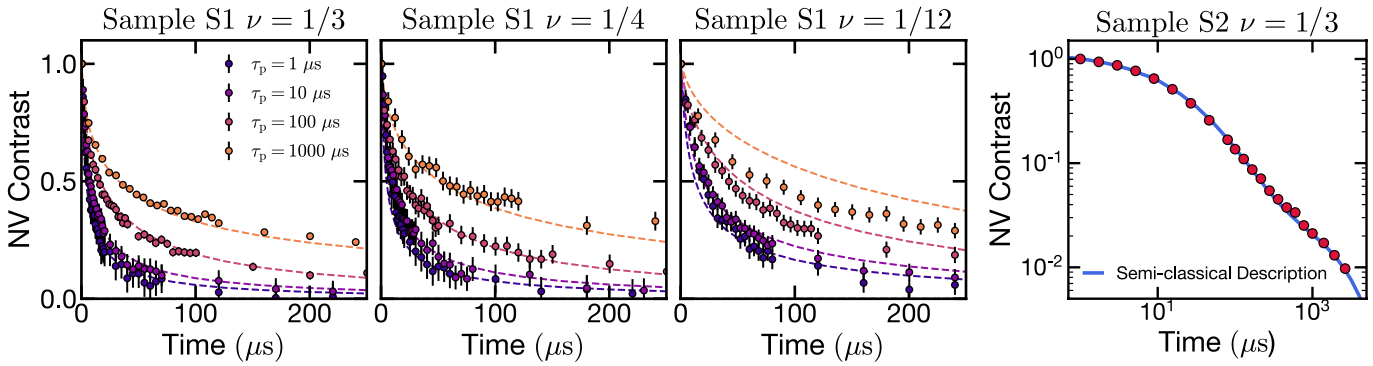

Extended Data Fig. 5 | Agreement between semiclassical model and experimentally observed dynamics. Given the approximately equal P1 density of both the sample S1 and S2, we simulate the the dynamics of a single NV defect surrounded by $N_{P1s} = \{300, 225, 75\}$ P1 centres for the groups $\nu = \{1/3, 1/4, 1/12\}$, respectively. In the polarization protocol, we choose $\Gamma_p = 0.1\,\mu s^{-1}$ for S1 and $\Gamma_p = 0.25\,\mu s^{-1}$ for S2. The subsequent polarization dynamics of the NV centre is given by the difference in populations between the $|0\rangle$ and $|-1\rangle$ states. For the $\nu \in \{1/3, 1/4\}$ groups of S1, we observe excellent agreement with the experimental data for over four orders of magnitude in τ_p and throughout then entire experimental timescale using $\gamma = 0.5\,\mu s^{-1}$. For the $\nu = 1/12$ group of S1, we observe good agreement, albeit with a smaller range of τ_p and using $\gamma = 1.5\,\mu s^{-1}$. We believe this discrepancy arises from a much larger separation between the strength of the on-site fields and the flip-flop rate of the ensemble. For the $\nu = 1/3$ group of S2, we also observe excellent agreement throughout the entire dynamics, where we use $\gamma = 0.3\,\mu s^{-1}$. The agreement observed in the NV polarization decay in both samples gives us confidence that our semiclassical model can capture the polarization dynamics in the sample and provide an accurate calculation of the diffusive properties of the spin ensemble.

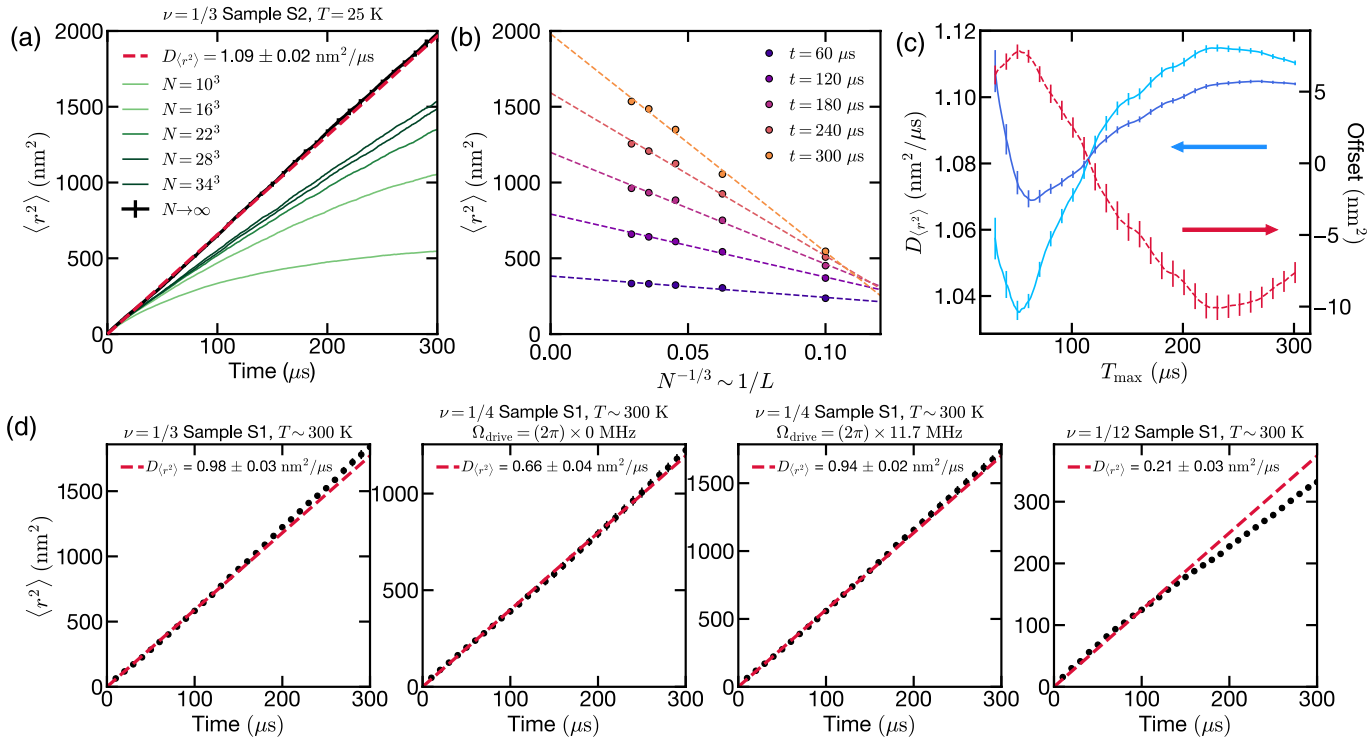

Extended Data Fig. 6 | Summary of extraction of diffusion coefficient. **a**–**c**, Extraction of diffusion coefficient of sample S2 at low temperature. **a**, Growth of $\langle r^2 \rangle$ for different system sizes N and the infinite system scaling (black line). **b**, Finite size scaling of $\langle r^2 \rangle$ to $N \to \infty$ assuming a linear in $L^{-1} \approx N^{-1/3}$ correction for representative values of t. **c**, Fitting the early-time growth of $\langle r^2 \rangle$ up to different times $T_{\max} \in [30, 300]$ leads to slightly different values of the diffusion coefficient, whether including a constant offset (light blue) or not (dark blue). Considering the fit without an offset, the final diffusion coefficient is taken to be the average with an uncertainty given by half the range of diffusion coefficients. **d**, For the different experimental conditions using the parameters discussed in Methods, we extract the diffusion coefficient from the growth of $\langle r^2 \rangle$, which is in great agreement with the experimentally extracted values after correcting for the non-Gaussian polarization profile (Table 1).

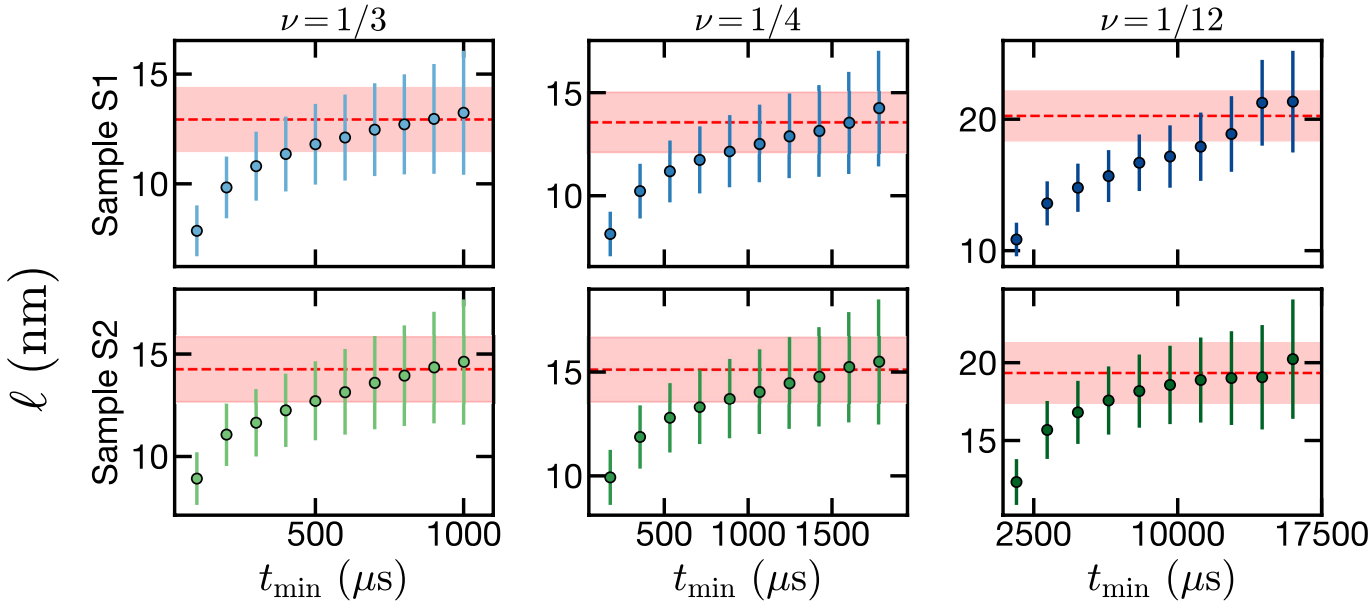

Extended Data Fig. 7 | Determination of the length scale ℓ. Extracted ℓ for different samples and different P1 groups as a function of the early time cut-off $t_{\min}$. Averaging over the last three data points, where the ℓ are consistent, yields the reported value of ℓ. The red dashed line corresponds to the final value and the shaded area is the associated uncertainty.

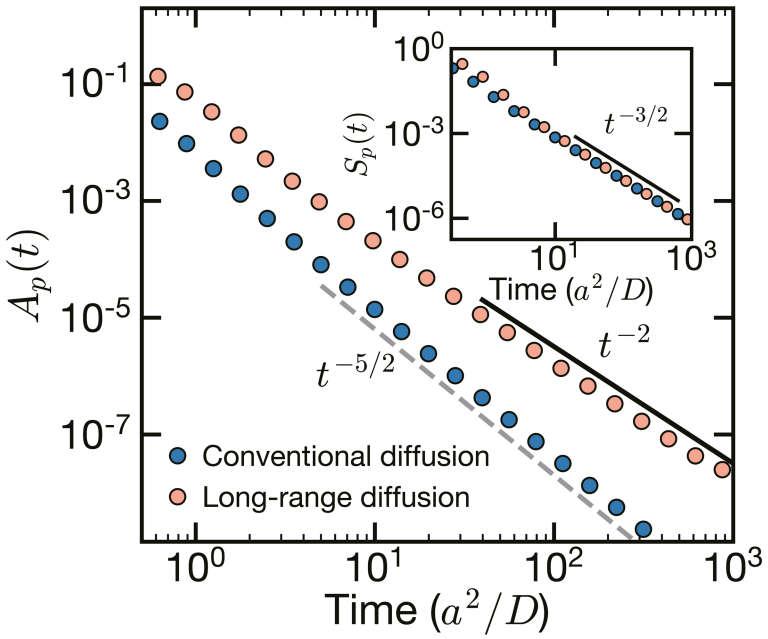

Extended Data Fig. 8 | Long-range modification to conventional diffusion. The presence of a long-range k^3-term parametrically modifies the approach, $A_p(t) = S_p(t) - (4\pi Dt)^{-3/2}$, to the late-time Gaussian fixed point, as high-lighted in a three-dimensional, disorder-less numerical simulation, with lattice constant a and diffusion coefficient D.

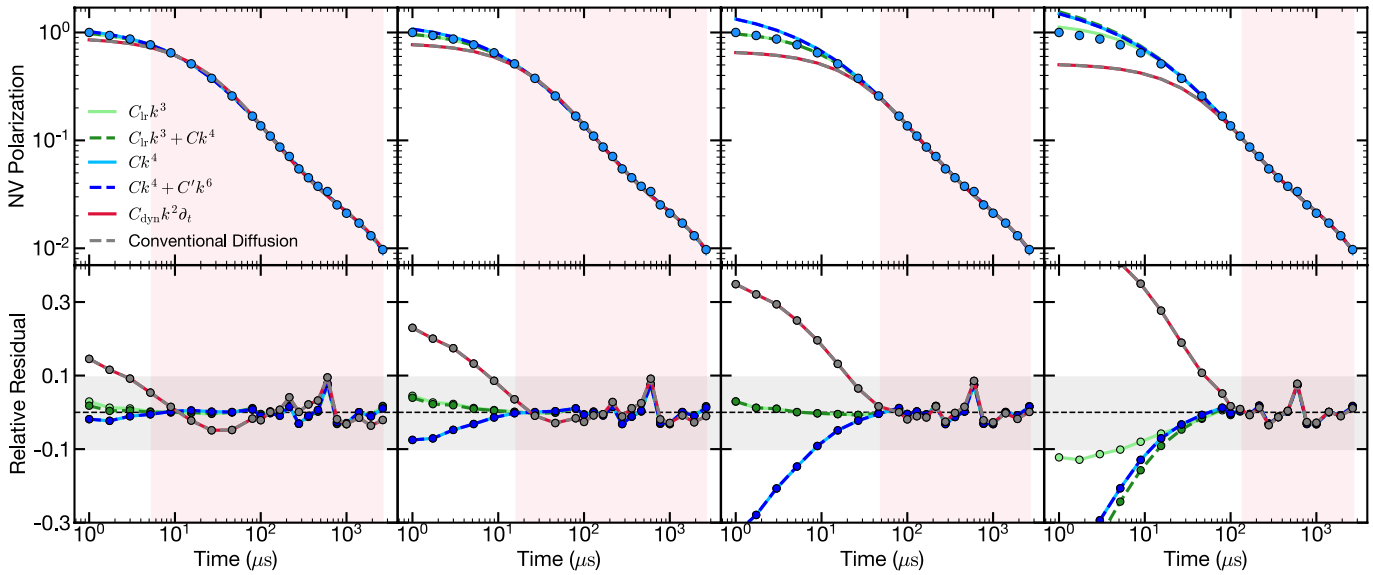

Extended Data Fig. 9 | Fitting of experimental data with different modifications to diffusion equation. Fitting of the diffusive description with different terms and fixed $T_1 = 2.6$ ms in sample S2 with $\tau_p = 30$ µs. Different columns represent fitting to a different range of the data (highlighted by the red shaded region). The inclusion of more terms in the diffusive description allows for a better fit of the data; however, the improvement in the fitting range is only significant when the fitting regimes includes early time data ($\lesssim$30 µs), as highlighted in the second row of the relative residuals. All data are presented with logarithmically spaced *y* axis, except in the grey shaded region where a linear regime is used to highlight the fluctuations of the residuals around 0. Fits in Fig. 1b correspond to the third column.

Extended Data Table 1 | Extracted ℓ from the spin polarization dynamics for the different sample considered (S1 and S2) and the different P1 subgroups

ℓ (nm)	$\nu = 1/3$	$\nu = 1/4$	$\nu = 1/12$
Sample S1	12.9 ± 1.4	13.6 ± 1.4	20.3 ± 1.9
Sample S2	14.3 ± 1.6	15.1 ± 1.5	19.3 ± 1.9

With decreasing density, we observe a corresponding increase in the lengthscale ℓ. Crucially, ℓ remains always larger than the P1–P1 distance, highlighting that its value is not a simple consequence of the discrete nature of the spins in our system. Note that to extract $\ell = \sqrt{C_{\mathrm{dyn}}}$, we must utilize our semiclassical model to obtain the full spatial profile of the polarization decay.